To appear in ApJ.
Preprint typeset using LaTeX style emulateapj v. 4/12/04

THE STAR FORMATION HISTORY OF THE VIRGO EARLY-TYPE GALAXY NGC 4435: THE *SPITZER* MID INFRARED VIEW.

P. Panuzzo[1], O. Vega[2], A. Bressan[1,2,4], L. Buson[1], M. Clemens[1], R. Rampazzo[1], L. Silva[3], J. R. Valdés[2], G. L. Granato[1,4], L. Danese[4]

To appear in ApJ.

ABSTRACT

We present a population synthesis study of NGC 4435, an early-type Virgo galaxy interacting with NGC 4438. We combine new spectroscopic observations obtained with the *Spitzer* Space Telescope IRS instrument with IRAC archival data and broad band data from the literature. The IRS spectrum shows prominent PAH features, low ionization emission lines and H_2 rotational lines arising from the dusty circumnuclear disk characterizing this galaxy. The central SED, from X-ray to radio, is well fitted by a model of an exponential burst superimposed on an old simple stellar population. From the lack of high excitation nebular lines, the [Ne III]15.5/[Ne II]12.8 ratio, the temperature of molecular hydrogen, and the fit to the full X-ray to radio SED we argue that the present activity of the galaxy is driven by star formation alone. The AGN contribution to the ionizing flux is constrained to be less than 2%. The age of the burst is found to be around 190 Myr and it is fully consistent with the notion that the star formation process has been triggered by the interaction with NGC 4438. The mass involved in the rejuvenation episode turns out to be less than 1.5% of the stellar galaxy mass sampled in a 5″ central aperture. This is enough to render NGC 4435 closely similar to a typical interacting early-type galaxy with inverted Ca II[H+K] lines that will later turn into a typical *cluster* E+A galaxy and enforces the notion that these objects are the result of a recent rejuvenation episode rather than a genuine delayed formation.

Subject headings: galaxies: elliptical — galaxies: evolution — galaxies: stellar content — galaxies: individual (NGC 4435)

1. INTRODUCTION

NGC 4435 (VCC1030), an early-type $SB0_1(7)$ galaxy (Sandage & Tamman 1981) member of the Virgo Cluster, is of great interest because it is a nearby example of galaxy interactions in the cluster environment. NGC 4435 is experiencing an off-center encounter with NGC 4438, a bulge dominated late-type galaxy lying at a projected separation of 4.3′ (i.e. 20 kpc, adopting a Virgo distance of 16.1 Mpc from Kelson et al. 2000). Evidence of the strong on-going interaction comes from the well developed stellar tidal tail (≈30 kpc) of NGC 4438 but also from the structure of the inter stellar medium (ISM) of both galaxies. Hα+[N II] images (Kenney et al. 1995) reveal several ionized gas filaments starting from the disk of NGC 4438 and extending out of the disk up to 10 kpc. The study of the distribution of the cold gas shows that CO and H I are displaced west of the center of NGC 4438, although CO is present also in the center of NGC 4435. Vollmer et al. (2005) proposed a model of the encounter based on the combined picture coming from the ISM observations and simulations. These latter authors indicate that the evolution of NGC 4438 has been influenced by its passage though the intra-cluster medium (ICM), where ram-pressure stripped the H I in about 100 Myr. During this period, NGC 4435 passed through the disk of NGC 4438 at high velocity (≈ 800 km s^{-1}), but the ISM-ISM interaction of the two galaxies had a less important effect on the final distribution of the gas than the cluster ram-pressure stripping exerted by the ICM.

If the above is the general picture of the NGC 4435/38 encounter, its effects on the evolution of NGC 4435 are less clear. In low density environments, Dominigue et al. (2003) showed that early-type galaxies show little or no IR or optical signatures of star formation when physically paired to a gas rich companion. However, some of the early-type members do show significant levels of IR and Hα emission that indicate both thermal (star formation) and non thermal (AGN) activity. These pairs are among the best candidates for direct interaction fueling of both starburst and active galactic nuclei.

NGC 4435 currently has an ISM. HST images reveal the presence of a circumnuclear disk of 4″ radius (360 pc, inclination 44 deg; Ho et al. 2002; Capetti & Balmaverde 2005). Moreover, nebular emission lines were detected by several authors (Kenney et al. 1995; Ho et al. 1995, 1997); in particular Ho et al. (1997), using the classical diagnostic diagrams, classified this galaxy as T2/H:, i.e. a transition object between LINER 2 and H II.

Coccato et al. (2006) studied the ionized gas kinematics using HST-STIS in the central 2″ looking for a super massive black hole (SMBH). The rotation curve is very symmetric, indicating a regular rotation. Their analysis indicates that the mass of the SMBH (upper limit $7.5 \times 10^6\ M_\odot$) is lower than that expected from the $M_{\rm BH}$-

[1] INAF Osservatorio Astronomico di Padova, vicolo dell'Osservatorio 5, 35122 Padova, Italy; pasquale.panuzzo@oapd.inaf.it, alessandro.bressan@oapd.inaf.it, lucio.buson@oapd.inaf.it, marcel.clemens@oapd.inaf.it, gian-luigi.granato@oapd.inaf.it, roberto.rampazzo@oapd.inaf.it
[2] Instituto Nacional de Astrofísica, Optica y Electrónica, Apdos. Postales 51 y 216, C.P. 72000 Puebla, Pue., México; ovega@inaoep.mx, jvaldes@inaoep.mx
[3] INAF Osservatorio Astronomico di Trieste, Via Tiepolo 11, I-34131 Trieste, Italy; silva@oats.inaf.it
[4] Scuola Internazionale Superiore de Studi Avanzati (SISSA), via Beirut 4, 34014, Trieste, Italy; danese@sissa.it

σ and $M_{\rm BH}$-$L_{\rm bulge}$ relations. Coccato et al. suggest that the SMBH in NGC 4435 could be of the "laggard" type as discussed in Vittorini et al. (2005), although these seem to lurk among galaxies that spend most of their lifetime in the field, at least apparently at odds with NGC 4435's cluster location.

In this paper we study the *Spitzer* IRS MIR spectra of NGC 4435 presented in Bressan et al. (2006) and perform a comprehensive analysis of the entire SED of the galaxy. In particular, the study of the MIR region, rich in spectral features (emission lines, PAH, dust emission etc.) provides an independent view of the nature of the nuclear activity of this galaxy (Genzel et al. 1998; Lutz et al. 1998; Roussel et al. 2001). Combined with the analysis of the panchromatic SED, it allows the characterization of the star formation activity and the estimate of the mass of stars formed during this interaction, shedding light on the rejuvenation mechanism in interacting early-type galaxies.

The paper is organized as follows. In § 2 we provide details of the observations and data reduction methods. In § 3 we describe the results of the study of the spectrum in the MIR region, while in § 4 we extend the modeling to the entire galaxy SED. In § 5 we discuss the result of our analysis and compare them with other studies. Finally in § 6 we summarize the conclusions.

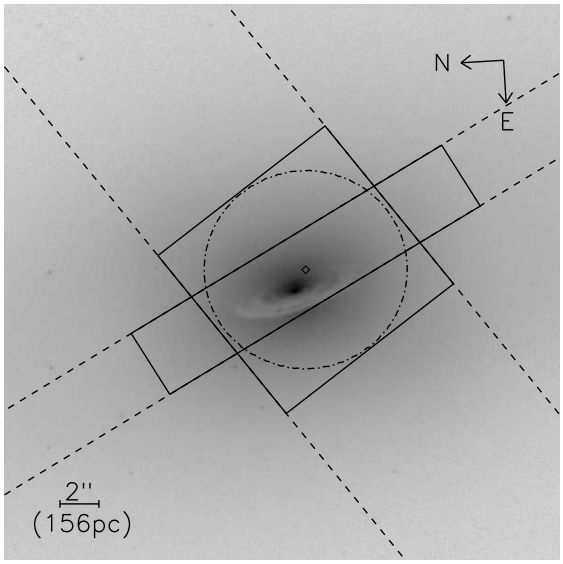

FIG. 1.— HST WFPC2/F814W image of the NGC 4435 nucleus (Coccato et al. 2006) with IRS SL and LL slits (dashed lines) during our observations. The rectangles show the aperture used to extract the spectrum. The dot-dashed circle shows the 5″ circular aperture used to define the SED of the central region from broad band data (see Sec. 4).

2. OBSERVATIONS AND DATA REDUCTION

2.1. *IRS spectra*

Spitzer IRS spectral observations of NGC 4435 were obtained during the first *Spitzer* General Observer Cycle on 2005 June 1 as part of a program (ID 3419, Bressan et al. 2006) to study early-type galaxies that belong to the colour – magnitude relation of the Virgo cluster (Bower et al. 1992).

The observations were performed in Standard Staring mode with low resolution ($R \sim 64$–128) modules SL1 (7.5–15.3μm), SL2 (5–7.6μm) and LL2 (14.1–21.3μm), with 6 exposures of 60 seconds for each SL module and 10 exposures of 120 seconds for the LL2 module.

Since the adopted IRS pipeline (version S12) is specifically designed for point source flux extraction, we have devised a new procedure to flux calibrate the spectra that exploits the large degree of symmetry that characterizes the light distribution in early-type galaxies. The reduction procedure is described in detail in Bressan et al. (2006) thus here we only summarize the main steps.

For SL observations, the sky background was removed by subtracting observations taken in different orders, but at the same node position. LL segments were sky-subtracted by differencing the two nod positions.

We obtained new e^-/s to Jy flux conversions by applying a correction for aperture losses (ALCF) and a correction for slit losses (SLCF) to the flux conversion tables provided by the Spitzer Science Center (e.g. Kennicutt et al. 2003). By applying the ALCF and SLCF corrections, we obtained the flux *received* by the slit.

For each galaxy of the program, we simulated the corresponding observed linear profile along the slits by convolving a wavelength dependent bidimensional intrinsic surface brightness profile with the instrumental point spread function (PSF). The adopted profile is a two dimensional modified King law (Elson et al. 1987). By fitting the observed profiles with the simulated ones, we can reconstruct the intrinsic profiles and the corresponding intrinsic SED. This procedure has also the advantage to recognize whether a particular feature is spatially extended or not.

Finally the spectrum was extracted in a fixed width (18″ for SL and 10.2″ for LL) around the maximum intensity. In order to account for the different extraction area, the LL spectrum has been rescaled to match that of SL (3.6″×18″). In Figure 1 we overplot the extraction area and the IRS slit positions on an HST WFPC2/F814W image of the NGC 4435 nucleus by Coccato et al. (2006).

The uncertainty on the flux was evaluated by considering two sources of noise: the instrumental plus background noise and the poissonian noise of the source. The former was evaluated by measuring the variance of pixel values in background-subtracted coadded images far from the source. The poissonian noise of the sources was estimated as the square root of the ratio between the variance of the number of e^- extracted per pixel in each exposure, and the number of the exposures. The total noise was obtained by summing the two sources in quadrature and by multiplying by the square root of the extraction width in pixels. We notice that the overall absolute photometric uncertainty of IRS is 10%, while the slope deviation within a single segment (affecting all spectra in the same way) is less than 3% (see the Spitzer Observer Manual).

2.2. *IRAC and MIPS images*

IRAC and MIPS images of NGC 4435 were retrieved from the SSC archive. They were taken as part of the program ID 3649. Fluxes at 3.6, 4.5, 5.8 and 8 μm were measured from the IRAC images as output from the "post-BCD" pipeline. The proximity of NGC 4435

to NGC 4438 results in a weak contaminating flux component. This was treated by estimating the median background flux from the image containing NGC 4435 so that the subtracted background included the contaminating light. Fluxes were extracted in circular apertures centered on the brightest pixel at each wavelength. Given that the calibration of extended sources for IRAC is still somewhat uncertain the fluxes so extracted have errors of $\sim 10\%$ (Dale et al. 2005). Similarly, we measured fluxes at 24, 70 and 160 μm from MIPS mosaics as output from the "post-BCD" pipeline. Fluxes were extracted in circular apertures centered on the brightest pixel at each wavelength, subtracting the median background flux measured far from the source. Uncertainties for MIPS fluxes are quoted to be $\sim 20\%$ (Dale et al. 2005, see also the Spitzer Observer Manual). It is worth noting that in all MIPS images the galaxy appares almost as a point source; in particular at 24 μm where the angular resolution is higest the galaxy image is only slightly larger than the instrumental PSF ($6''$).

3. ANALYSIS OF THE MID-IR SPECTRUM

The final flux calibrated IRS spectrum of NGC 4435 is shown in the top-left panel of Figure 3. The spectrum is dominated by numerous PAH features and shows several nebular emission lines, [Ar II]7μm, [Ne II]12.8μm, [Ne III]15.5μm and [S III]18.7μm, and molecular hydrogen rotational lines, H_2 S(3) 9.66μm, H_2 S(1) 17.04μm.

In order to measure the fluxes of emission lines and to identify the PAH features, we fitted the spectrum via decomposition into various components: PAH emission features, emission lines and underlying continuum.

For all the PAH features but those at 11.2 and 12.5 μm, we assumed a Drude profile. The features at 11.2 and 12.5 μm are very asymmetric thus we have used the profiles observed by Hony et al. (2001), convolved to the SL1 resolution. It is worth noticing that the emission profiles derived by Hony et al. (2001) do not account for the blending of the wings of the PAH features. Consequently our underlying continuum shows a broad feature. However, since the main purpose of this section is to estimate the emission line intensities, this does not affect our conclusions.

For the emission lines we adopted a Gaussian profile, with a FWHM given by the resolving power of the corresponding IRS module (see the *Spitzer* Observer's Manual, v. 6.0, sec. 7.1.6). The resulting fits of the three most interesting spectral regions are shown in Figure 3.

3.1. *PAH features*

In the IRS spectrum of NGC 4435 we can identify many PAH emission features already known from ISO and pre-ISO studies: at 6.2, 7.7, 8.2, 8.6, 11.2, 11.9, 12.7, 13.5, 14.5, 15.9, 16.4 μm (e.g. Li & Draine 2001; Sturm et al. 2000). Besides those features, we also see a number of new components that have been revealed by recent *Spitzer* observations. These are the feature at 10.7 μm and, most notably, the complex around 17 μm. The nature of the former is unknown but there is similar evidence in M82 (Förster Schreiber et al. 2004), NGC 7714 (Brandl et al. 2004) and NGC 7331 (Smith et al. 2004) spectra. The complex around 17 μm (Figure 3, bottom-right panel) is similar to that observed in the spiral galaxies NGC 7331 and in the extended emission of M82 (Engelbracht et al. 2006). This complex is superimposed on H_2 S(1) emission but in our case, since the H_2 S(1) emission is fainter than that seen in NGC 7331 and M82, we can more accurately extract the underlying emission components. In fact, while Smith et al. (2004) claimed the presence of a new broad emission feature at 17.1 μm with a FWHM of 0.96 μm, in our spectrum this feature appears to be a blend of two components; a narrow component centered at 17.4 μm with a FWHM of 0.33 μm and a broad component centered at 16.9 μm with a FWHM of 1.1 μm. Notice that the component centered at 17.4 μm was observed by Van Kerckhoven et al. (2000) in various galactic star formation regions. Thus our observations indicate that the new PAH emission feature is centered at 16.9 μm. In the same spectral region we also find an emission feature at 19.07 μm that was observed in the NCG 7023 reflection nebula by Werner et al. (2004).

TABLE 1
Emission line intensities.

Transition/Ion	$\lambda_{\rm rest}$ (μm)	Flux (10^{-17} W m^{-2})
H_2 0–0 S(5)	6.9095	0.505 ± 0.411
[Ar II]	6.9853	3.787 ± 0.378
H Pfα	7.4599	1.567[a]
H_2 0–0 S(3)	9.6649	1.055 ± 0.288
[Ne II]	12.8136	6.972 ± 0.252
[Ne III]	15.5551	2.666 ± 0.168
H_2 0–0 S(1)	17.0348	1.808 ± 0.163
[S III]	18.7130	2.248 ± 0.119
[Fe II]	5.3402	< 1.92
H_2 0–0 S(7)	5.5112	< 1.76
H_2 0–0 S(4)	8.0250	< 1.53
[Ar III]	8.9914	< 1.03
[S IV]	10.5105	< 0.60
H_2 0–0 S(2)	12.2786	< 0.96
[Ne V]	14.3217	< 0.41
[Fe II]	17.9360	< 0.34

[a]We quote here the measurement of Pfα intensity provided by the fitting procedure, however its value is unreliable because it falls in the wing of the broad PAH 7.7 μm emission feature.

3.2. *Emission lines*

In the MIR spectrum of NGC 4435 we detect only low ionization emission lines. The corresponding intensities are listed in table 1. The reported uncertainties in the line fluxes are 1σ as derived from the line fitting. For some interesting higher excitation emission lines we can only provide 3σ upper limits. In the following we discuss the main implications of our detections.

3.2.1. *Constraints on AGN excitation*

Nebular emission lines provide a powerful diagnostic tool to determine the nature of the source of energy powering the emission. Classically, the determination is done using optical emission lines. Optical spectra of the nuclear region of NGC 4435 were observed by Ho et al. (1995). Using the diagnostic diagrams of Veilleux & Osterbrock (1987), Ho et al. (1997) classified NGC 4435 as a transition object between LINER and H II, via the value of [O I]6300/Hα (=0.13) which, however, has an uncertainty of 30-50%. Revisiting the

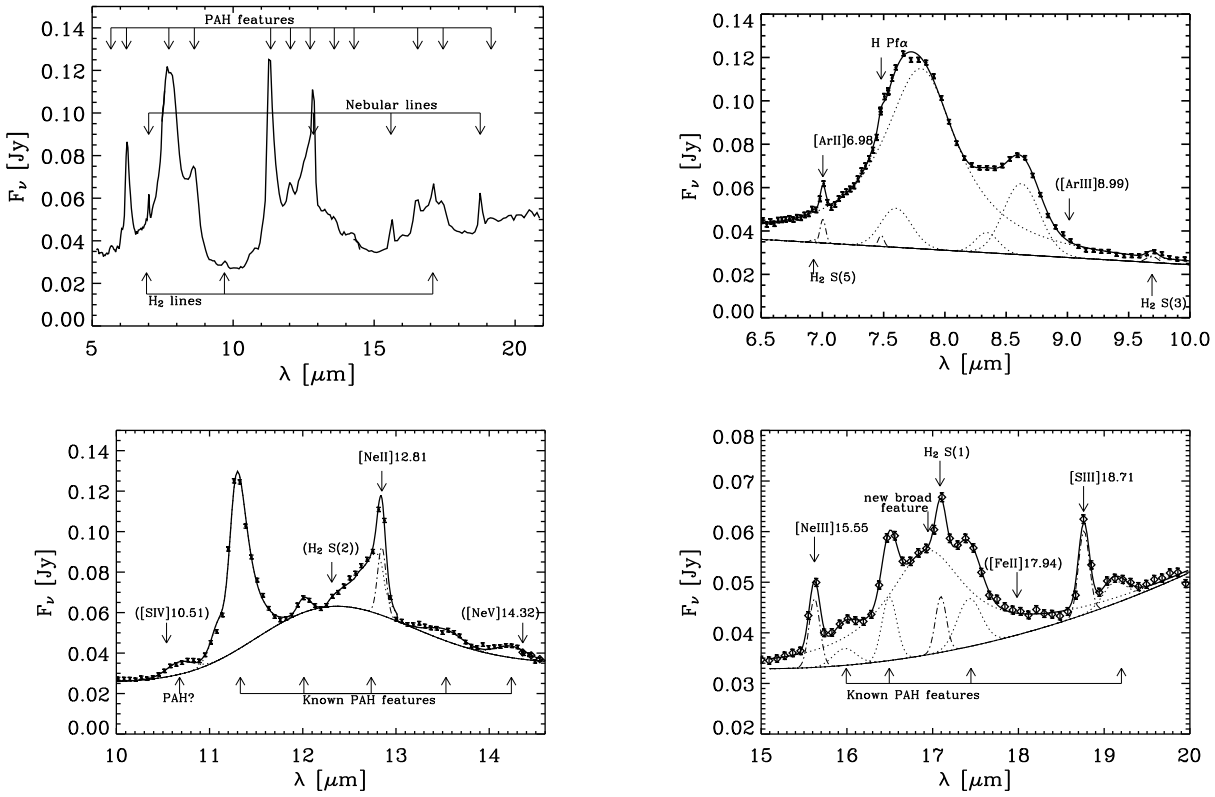

FIG. 2.— *Spitzer* IRS MIR spectrum of NGC 4435. *Top-left:* entire observed spectrum; arrows indicate the positions of PAH features, nebular emission lines and H_2 rotational lines. *Top-right:* the 6.5–10μm spectral region split in the different components. The error bars correspond to 1 σ noise fluctuations. The lower smooth solid line corresponds to the continuum component; the dotted line to the continuum plus PAH features, the dot-dashed lines show the continuum plus emission lines. Finally the upper solid line represents the sum of all components. Lines for which we could provide only upper limits are included in parenthesis. *Bottom-left:* similar to top-right panel but for the 10-14.6μm spectral region. *Bottom-right:* similar to top-right panel but for the 15-20μm spectral region.

classification using the AGN/H II separation proposed by Kewley et al. (2001), the [O I]6300/Hα ratio is only marginally larger than that expected for H II regions.

The IRS spectrum allows us to make use of the ratio [Ne III]15.5/[Ne II]12.8 which is a strong infrared diagnostic for the hardness of the ionizing source. We compared the observed ratio of [Ne III]15.5/[Ne II]12.8=0.38 with CLOUDY models (Ferland et al. 1998). We computed several photoionization models using as ionizing source the spectrum of a 35000 K star (with Kurucz atmosphere model) plus a 10^5 K blackbody, representing the AGN contribution (a similar test was done by Lutz et al. 1998). Assuming an ionization parameter $\log(U) = -2$, and $n_H = 70$ (derived from S II optical lines), the observed ratio [Ne III]15.5/[Ne II]12.8 limits the AGN contribution to the ionizing flux to be less than 2%.

3.2.2. *H_2 rotational emission*

In Table 1 we provide the intensity of detected H_2 rotational emission lines.

The first excited rotational state of H_2 that can provide a transition toward the fundamental level has an angular moment $J = 2$ and an energy of 510 K, thus the H_2 does not radiate for temperatures typical of the cold molecular medium (some 10 K) but only for temperatures above 100 K. The investigation of the state of warm molecular gas can be done using the excitation diagram, shown in Figure 3.2.2, where the natural logarithm of the number of molecules in the state i (N_i) divided by the statistical weight of the state (g_i) is plotted against the energy (E_i) of the excited state with respect to the ground state. The

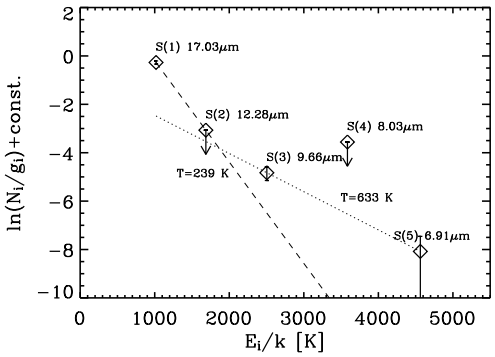

FIG. 3.— Excitation diagram for H_2 rotational lines observed in the NGC 4435 IRS spectrum. Diamonds show the natural logarithm of the number of molecules in the state i computed with eq. 1 divided by the statistical weight plotted versus the energy of the excited state with respect to the ground state. Error bars represent 1σ errors on line intensity, while arrows show upper limits on H_2 S(4) and H_2 S(2) lines. The dashed and dotted lines show the fits to the warm and hot components, respectively.

number of molecules in state i is given by (assuming a density smaller than the critical density):

$$N_i = \frac{L_i}{A_i h\nu_i} \quad (1)$$

where L_i is the luminosity of the line emitted by the transition starting from the state i, A_i is the transition probability, and ν_i the frequency of the transition.

Assuming local thermal equilibrium, the ratio between number of molecules in state i and the total number of H_2 molecules per unit of volume is given by the Boltzmann equation (Parmar et al. 1991):

$$\frac{n_i}{n_{H_2}} = g_i \frac{hcB}{2kT} \exp\left(-\frac{E_i}{kT}\right) \quad (2)$$

where B is the H_2 rotational constant.

For an isothermal gas all the data in the excitation diagram of Figure 3.2.2 should lay on a linear relation $y = a + bx$ with $b = -1/T$. However, the observed values do not lay on the same line, suggesting the presence of two (or more) components at different temperatures, a "warm" component at $T \leq 240$ K traced by the S(1) line (and the S(2) upper limit) and a "hot" component at $T \simeq 630$ K, traced by lines at shorter wavelengths. With equations 1 and 2 we can estimate the mass of the "warm" and "hot" components. Assuming a temperature of 200 K for the warm component, we find a mass of $6.3 \times 10^4 M_\odot$, while for the "hot" component we find a mass of $7.1 \times 10^3 M_\odot$.

The excitation mechanism for hot and warm molecular gas in galaxies is commonly attributed to UV flux from young stars in photodissociation regions (PDR), shocks or X-ray flux from an active nucleus (Burton et al. 1992; Rigopoulou et al. 2002).

The upper limit on the temperature derived from S(1) and S(2) lines excludes AGN excitation. In fact Rigopoulou et al. (2002) find that in Seyfert galaxies the temperature from these lines is typically around 350 K. Indeed, the temperature we find is compatible with PDR models by Burton et al. (1992). Finally, it is worth noting that the mass of the warm gas is only a tiny fraction ($\sim 0.06\%$) of the total molecular gas observed in NGC 4435 from CO lines ($\sim 10^8 M_\odot$, Vollmer et al. 2005). This fraction is also significantly smaller than that found in typical powerful starbursts (1 – 10%) or in Seyfert galaxies (up to 30%, Rigopoulou et al. 2002). This is consistent with our finding that the star formation in NGC 4435 has already declined and is more characteristic of a post-starburst phase, as we discuss in the following sections.

Note that the above values are not corrected for dust attenuation. However, the attenuation we derived from the model fit to the global SED in the following sections is quite low ($A_\lambda \sim 0.1 - 0.2$) at these wavelengths.

3.2.3. *Abundance determinations*

From the intensity of the Pfα, neon and argon lines we could obtain an estimate of the metallicity of the ionized gas, following the procedure outlined in Verma et al. (2003). In fact, for a generic element X and as long as the current density is lower than the critical density for collisional de-excitation of the involved transitions, the abundance relative to hydrogen is given by:

$$\frac{\mathrm{X}}{\mathrm{H}} = \frac{j_{\mathrm{Pf}\alpha}}{F_{\mathrm{Pf}\alpha}} \left(\frac{F_{[\mathrm{XII}]}}{q_{[\mathrm{XII}]} h\nu_{[\mathrm{XII}]}} + \frac{F_{[\mathrm{XIII}]}}{q_{[\mathrm{XIII}]} h\nu_{[\mathrm{XIII}]}} + ... \right) \quad (3)$$

where $j_{\mathrm{Pf}\alpha}$ is the emissivity for the Pfα, and $q_{[\mathrm{XII}]}$ is the collisional excitation rate of [X II] transition (for electronic density near to zero). The above abundances can be translated into metallicity estimations by dividing them by standard ISM abundances.

We notice however that, while we are confident on the determination of metal line intensities, the Pfα falls in the wing of a broad PAH emission feature. The measurement of Pfα intensity is thus unreliable, even if the fitting procedure gives a small uncertainty (reported in table 1). For this reason we do not proceed with a direct determination of the abundances in this way. However an alternative way to exploit the good measurements of metallic lines in order to derive the metallicity is to use the hydrogen line intensity as predicted from the fit to the global SED of the galaxy. This will be discussed in a following section.

4. ANALYSIS OF THE PANCHROMATIC SED

The analysis of the MIR spectrum made in the previous section indicates that a star formation activity is present in the circumnuclear disk of NGC 4435. In order to better characterize the emission mechanisms and the stellar population content of this galaxy we will model the panchromatic SED of NGC 4435 by means of our spectro-photometric code GRASIL[5] with the recently updated treatment of PAH emission based on ISO data (for details on GRASIL see Silva et al. 1998; Silva 1999; Granato et al. 2000; Bressan et al. 2002; Panuzzo et al. 2003, 2005; Vega et al. 2005).

The panchromatic SED was constructed by combining the IRS spectra (including the main nebular lines) with archival data matching as far as possible the IRS apertures. J, H and Ks fluxes within an aperture of 5″ radius were taken from the 2MASS database at IRSA[6]. IRAC fluxes in the 3.6, 4.5, 5.8, and 8.0 μm bands were extracted in the same aperture from archival images as explained in section 2.2. IRAS 60, and 100 μm fluxes (obtained from NED) were used to define the FIR SED together with MIPS total fluxes. Although the apertures of MIPS and IRAS are larger than the IRS aperture, the above fluxes are dominated by emission from the dusty circumnuclear disk as clearly shown by the 24 μm MIPS image. This is not true, however, at 12 μm, where we expect a significant contribution from the old stellar population; thus the 12 μm IRAS flux has not been included in the SED. We also excluded the IRAS 25 μm flux (0.22 Jy, from NED) because it is not compatible with the 24 μm MIPS flux; this is probably due to an incorrect background subtraction due to the poor resolution of IRAS. Radio data were taken from Nagar et al. (2000), Wrobel & Heenschen (1991), Becker et al. (1991), Dressel & Condon (1978),

[5] Available at http://adlibitum.oats.inaf.it/silva/default.html or http://web.oapd.inaf.it/granato/grasil.html

[6] The NASA/IPAC Infrared Science Archive is operated by the Jet Propulsion Laboratory, California Institute of Technology, under contract with the National Aeronautics and Space Administration.

TABLE 2
Broad band fluxes of NGC 4435 applicable for 5″ central region

λ (μm)	Band / Instrument	Flux (Jy)	Uncert. (mJy)	Ref.
1.25	J	0.11	12.1	1
1.65	H	0.14	15.3	1
2.17	Ks	0.12	13.2	1
3.6	IRAC	0.056	5.6	2
4.5	IRAC	0.033	3.3	2
5.8	IRAC	0.039	3.9	2
8.0	IRAC	0.062	6.2	2
23.7	MIPS	0.11	22.0	2
60	IRAS	1.99	597.0	3
71.0	MIPS	2.27	454.0	2
100	IRAS	4.68	1404.0	3
156	MIPS	3.7	740.0	2
20000	VLA	<0.0011	-	4
60000	VLA	>0.0012	-	5
61856		<0.007	-	6
126050		<0.004	-	7
200000	VLA	0.0022	0.216	8

References. — (1) IRSA; (2) this work; (3) NED; (4) Nagar et al. 2000; (5) Wrobel & Heeschen 1991; (6) Becker et al. 1991; (7) Dressel& Condon 1978; (8) FIRST VLA survey.

and the FIRST-VLA survey. The SED is completed with GALEX UV fluxes extracted within a 5″ aperture (Boselli & Cortese, private communication). The broad band fluxes are given in Table 2.

4.1. *The models*

Since the broad band SED obtained in the previous section is produced by the star-forming circumnuclear disk and the old population, including also the stars seen in projection, we adopted a simple composite model for the fit: a starburst plus an old stellar population. The old stars are modelled as an unattenuated simple stellar population (SSP) with given age and metallicity. The SSPs are based on Padova stellar models and include the contribution from dusty circumstellar envelopes around asymptotic giant branch stars. This fact may be relevant because these old stars leave an excess around 10 μm (Bressan et al. 1998, 2001, 2006).

The starburst contribution was modelled with GRASIL assuming different values for the age ($t_{\rm b}$), metallicity and star formation history. The latter was assumed as an exponentially decreasing SFR parameterized by the e-folding time, $\tau_{\rm b}$. We consider two phases for the ISM: the molecular clouds (MCs) which surround young star clusters and the diffuse component. For the distribution of both the diffuse ISM and stars we adopted a disk geometry, with an inclination of 45° with respect to the line-of-sight (as suggested by observations, e.g. Coccato et al. 2006). The density of dust and stars is assumed to be exponential in both radial and vertical direction, with different scales for dust and stars (see Silva et al. 1998, for more details).

Among the GRASIL physical quantities that mostly affect the shape of the SED we recall *(i)* the total gas mass $M_{\rm gas}$, *(ii)* the fraction of molecular mass[7] to total gas mass ($M_{\rm mol}/M_{\rm gas}$), *(iii)* the optical depth of molecular clouds at 1μm (τ_1), and *(iv)* the escape time-scale of newly born stars from their parent MCs ($t_{\rm esc}$). The dust composition and optical properties are set to reproduce the extinction and emission properties observed in the diffuse ISM of our Galaxy. The gas-to-dust mass ratio (G/D) is set proportional to the metallicity (Z), with $G/D = 110$ for solar metallicity.

[7] In the GRASIL model we identify the molecular gas with the clouds surrounding young star clusters. Molecular gas could also be present in the diffuse component but the code doesn't differentiate between atomic and molecular gas in this phase.

TABLE 3
Parameters for the burst model library.

$\tau_{\rm b}$ (Myr)	$\log(t_{\rm b})$ (yr)	$t_{\rm esc}$ (Myr)	$M_{\rm mol}/M_{\rm gas}$	τ_1
10 - 100	6.0 - 8.8	1 - 99	0.10 - 0.99	0.01 - 180

TABLE 4
Best fit parameters for the burst model.

$\tau_{\rm b}$ (Myr)	$t_{\rm b}$ (Myr)	Z (Myr)	$t_{\rm esc}$	$M_{\rm mol}/M_{\rm gas}$	τ_1
55	186	0.02	3.0	0.20	0.25

For the nebular lines we adopted the large H II region library computed by Panuzzo et al. (2003). Finally, the adopted IMF is a Salpeter IMF (Salpeter 1955) in the mass range from 0.1 to 100 $M_\odot$.

4.2. *Results of the SED fit*

We computed a large grid of simulated SED with GRASIL. In Table 3 we list the ranges of values used for the library. Among these models, we identified the best fitting model as the one that maximize a likelihood function. The likelihood function was built using UV, MIPS, IRAS and radio data and their uncertainties quoted in Table 2 and the intesities of observed line Hα, Hβ (from Ho et al. 1997) and [Ne II]12.8μm. The best fit model is shown in Figure 4.2, where the left panel shows the panchromatic fit, from the UV to radio wavelengths, while the right panel is a zoom into the MIR spectral region. The corresponding parameters and some important derived quantities are displayed in Tables 4 and 5 respectively.

The wide wavelength coverage of the SED imposes strong constraints to the model, because different spectral regions probe the age sequence of the stellar populations. Broadly speaking, nebular emission lines are dominated by massive stars, radio emission is contributed by stars younger than about 50 Myr while the FIR SED includes also a significant contribution from intermediate mass stars. The UV/FIR ratio implies that the burst luminosity is almost completely reprocessed by dust and emitted in the FIR, thus the FIR luminosity fixes the bolometric luminosity of the burst. The emission line luminosities and radio fluxes constrain the star formation rate in the last 50 Myr determining the timescale $\tau_{\rm b}$. Once the current SFR and $\tau_{\rm b}$ are determined, the age of the burst is fixed by its luminosity. Finally, the Hα and Hβ constrain the attenuation at optical wavelenght (see

TABLE 5
Derived quantities of the SED models.

$M_{\star F}^{SB}$ ($M_\odot$)	M_{gas} ($M_\odot$)	$M_{old}^{5''}$ ($M_\odot$)	$L_{SB}^{5''}$ (%)	$L_{old}^{5''}$ (%)	$\langle SFR \rangle$ ($M_\odot$ yr^{-1})	SFR_c ($M_\odot$ yr^{-1})	A_V^{mod} (mag)
1.40×10^8	1.36×10^8	8.2×10^9	32.0	68.0	0.75	0.089	2.69

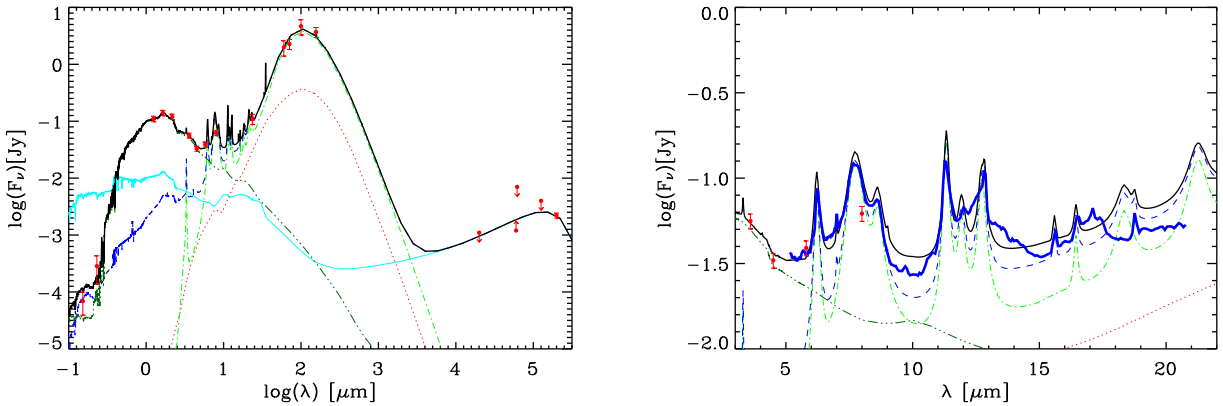

Fig. 4.— Comparison between the observed SED of the central region of NGC 4435 and our model. The thick solid black line represents the model for the total SED, i.e. the starburst component plus the old stellar component; the three dots-dashed darkgreen line represents the contribution from the old stellar population, and the dashed blue line represents the total contribution from the burst of star formation, the dotted red line represents the emission from molecular clouds. The dot-dashed green line represents the diffuse medium emission and the thin cyan solid line denotes the emission from stars of the starburst component without applying the extinction from dust. The red-filled circles are the broad band data. *Left*: Comparison from 0.1μm to 100 MHz. *Right*: Comparison for the MIR wavelengths. The thickest blue solid line represents the IRS *Spitzer* spectrum.

section 5.2 for more details).

Our assumption of an exponentially declining SFR is the simplest model consistent with a Schmidt-type law that reproduces the multiwavelength SED. Other more complex scenarios could probably be able to fit the data introducing, however, further free parameters that are not justified. Indeed, stars in the obscured burst older than $\sim$ 50 Myr do not provide observable "features" to disentangle the detailed shape of the star formation history.

It is also interesting to consider the effects of a underlying star formation activity already present in NGC 4435 before the interaction (i.e. older than $\sim$ 200 Myr). Stars originated from this activity would unlikely remain confined to the dusty disk. For example in our galaxy, stars older than 150 Myr show larger spatial distribution than younger stars (Robin et al. 2003; Panuzzo et al. 2006). Thus the intermediate age stars would now be mostly outside the dusty disk and, as a consequence, they would suffer from only a small or negligiable attenuation. Since stars 200–500 Myr old are still important emitters at UV wavelengths, they would contribute significantly to the GALEX fluxes. However, the measured UV GALEX and NIR fluxes within the 5$''$ aperture (Fig. 4.2 left panel), are already entirely accounted for by the old population and the obscured starburst. Actually, the observed FUV flux within the 5$''$ aperture corresponds to an activity not larger than SFR $\sim 3 \times 10^{-4} M_\odot$ yr^{-1} between 200 and 500 Myr ago. This suggests that no significant underlying intrinsic star formation activity was present and, consequently, that the observed burst was triggered by the interaction.

The old stellar population dominates the emission in the optical and NIR range but is significant also in the MIR. In fact we see from Figure 4.2 that the fractional contribution of the starburst to the IRS spectrum increases with wavelength. This is consistent with the results of the spatial analysis along the slit presented in section 2.1. We find that the continuum below $\sim$ 6 μm looks extended, while the emission at longer wavelengths (in particular the PAH features) looks unresolved, in agreement with the different concentration observed in ISO LW2 and LW3 images (Boselli et al. 2003), IRAC and MIPS images, as detailed below.

Finally we notice that the fit of the SED does not require an AGN component, which adds further support for the lack of AGN activity in NGC 4435.

In the following we discuss in more detail the results of the fit.

5. DISCUSSION

5.1. *The star formation history and starburst luminosity*

The old stellar component is well fitted by a solar metallicity SSP of 8 Gyr and a mass of 8.2×10^9 $M_\odot$. Note that the value here derived for the stellar mass depends on the adopted IMF. Coccato et al. (2006) give an estimate of the mass to light ratio (M/L) of the population that can be directly compared with our old stellar population. Using the I band they measured $M/L(I) = 2.2 \cdot M_\odot/L_\odot(I)$, while for our old stellar population it is $M/L(I) = 2.98 \cdot M_\odot/L_\odot(I)$. The discrepancy in the M/L can be solved by changing the slope of the IMF at lower masses (as in the Kroupa IMF, Kroupa

1998) or adopting a higher lower mass limit (e.g. 0.2 $M_\odot$) without changing the predicted SEDs.

The nuclear disk is in a post-starburst phase ($\tau_b = 55$ Myr and $t_b = 186$ Myr) with a current star formation rate ($SFR_c = 0.089\ M_\odot\ yr^{-1}$) about one order of magnitude smaller than the average star formation rate ($\langle SFR \rangle = 0.75\ M_\odot\ yr^{-1}$). The quality of radio data, however, prevents a determination of τ_b better than $\pm 20\%$; this results in an uncertainty on the age of the sturburst t_b of the same order. The mass of gas converted into stars during the burst is $M_{\star F}^{SB} = 1.40 \times 10^8\ M_\odot$; however with the adopted IMF, only $\sim 80\%$ still survive. The star forming component emits 32% of the bolometric luminosity in the central 5″ of the galaxy, while accounting for 1.4% of the stellar mass. Most of the starburst luminosity is provided by A stars, reprocessed by the diffuse dust and re-emitted in the 8-1000 μm spectral region ($L_{IR} \simeq 5.5 \times 10^{35}$ W).

A population of A stars in the central $\sim$ 550 pc has already been detected by optical observations (Kenney et al. 1995). More recently, Sarzi et al. (2005) estimated that the contribution of the young burst from 3000 Å to 5700 Å in the nuclear region (0.″13 radius) is around 12%. In the same spectral region we estimate that the fractional contribution of the starburst is only 6%. It is however hard to compare the two estimates because our value refers to a much larger region (5″). Indeed it is sufficient that in the very central region the attenuation be reduced (as estimated by Sarzi et al. 2005) to eliminate this discrepancy without affecting significantly the constraints from the other spectral bands.

The strongly declining SFR makes this galaxy a typical cases where different SFR indicators, probing different timescales, provide estimates that are apparently discrepant. In fact with the classical SFR estimation based on the IR luminosity provided by Kennicutt (1998) we get $SFR_{IR} = 0.25\ M_\odot\ yr^{-1}$, in between the average SFR and the current one. Using the 1.4 GHz flux with the Panuzzo et al. (2003) calibration we get $SFR_{1.4GHz} \simeq 0.117\ M_\odot\ yr^{-1}$. This value is more similar to the current SFR value than the IR based estimate because the radio emission is due to free-free emission from HII regions and synchrotron emission from core collapse supernovae.

5.2. *The geometry and the attenuation law*

Though the star formation history is well constrained by the fit of the total SED, a further refinement to the relative spatial distribution of stars and dust can be obtained by the comparison of the predicted and observed Hα and Hβ line intensities. It was shown in previous works that a system with an equal spatial distribution of stars and dust produces a much smaller reddening than a "screen" geometry (e.g. Witt & Gordon 2000). With the assumption of equal scales for stars and dust and given the strong attenuation implied by the observed UV/FIR ratio, the Hα intensity predicted by our best fit model would be much smaller than the observed value ($I(H\alpha) = 2.82\times10^{-17}$ W m^{-2}, Ho et al. 1997) and the predicted gas mass about twice the quoted value $\sim 10^8 M_\odot$ (Vollmer et al. 2005). To solve this discrepancy we need to decrease the attenuation in the optical band leaving unchanged that in the UV. Without modifying the optical properties of dust grains, this can be achieved by assuming a geometry where the diffuse dust is more extended than the stellar distribution. This has the effect of increasing the reddening, because it reddens the attenuation law making it more similar to the extinction of a uniform slab. Adopting a radial (vertical) scale length of 160 (22) pc for the diffuse dust and of 70 (14) pc for the stellar component the predicted intensities for Hα and Hβ are $I(H\alpha) = 2.70\times10^{-17}$ W m^{-2}, and $I(H\beta) = 4.99\times10^{-18}$ W m^{-2} well in agreement with the observed value (4.99×10^{-18} W m^{-2} for Hβ from Ho et al. 1997). The required dust mass is $1.23 \times 10^6\ M_\odot$. For a solar metallicity, as predicted by other observables discussed below, this implies a gas mass $M_G \sim 1.36 \times 10^8\ M_\odot$, fairly near to the observational value.

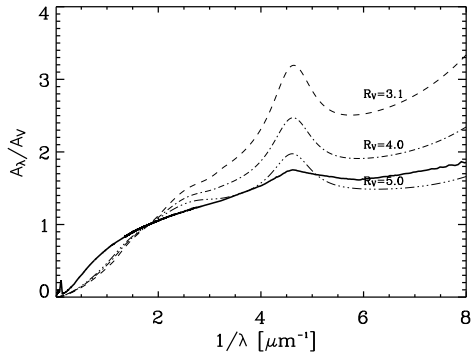

FIG. 5.— Comparison of Cardelli extinction curves with different R_V with the attenuation curve derived from the best fit model (solid line).

The estimated mean attenuation of the system in the V band is $A_V^{mod} = 2.69$ mags. The resulting attenuation law is shown in Figure 5. In the same figure we plot, for comparison, three different extinction curves from Cardelli et al. (1989). We stress that the dust properties adopted in the model are such that they reproduce the Galactic extinction law, corresponding to R_V=3.1. Thus the geometry of the model (including the effects of age dependent attenuation) produces an effective attenuation law which is very different from the adopted intrinsic extinction properties of the dust (Granato et al. 2000; Panuzzo et al. 2003, 2006).

5.3. *The gas and star metallicity*

The best fit to the NGC 4435 SED is obtained by adopting solar metallicity for both stars and gas in the starburst.

Following the detailed study of nebular emission models of Panuzzo et al. (2003) we can also compute the predicted intensities of selected emission lines. This is particularly useful for abundance determinations with infrared lines in the absence of good measurements of hydrogen recombination lines (see Panuzzo et al. 2003), as in the present case. In fact from the SFR obtained from the fit of the SED, GRASIL also computes the ionizing flux and thus, the observed intensity of the main emission lines. This can be considered as an alternative method to obtain the ionizing flux from a direct measurement of the hydrogen recombination lines. Adopting solar metallicity and standard ISM abundances we obtain the following predicted intensity: $I(Pf\alpha) = 3.46 \times 10^{-18}$

W m^{-2}, $I([\mathrm{Ne\,II}]) = 7.01 \times 10^{-17}$ W m^{-2}, $I([\mathrm{Ne\,III}]) = 2.60 \times 10^{-17}$ W m^{-2}, $I([\mathrm{Ar\,II}]) = 3.17 \times 10^{-17}$ W m^{-2} and $I([\mathrm{S\,II}]) = 1.71 \times 10^{-17}$ W m^{-2}. For the metallic lines these figures are in good agreement with the observed values reported in Table 1, thus providing an independent confirmation that the gas metallicity is solar. The value found for Pfα is much lower than that derived from the fit of the line, suggesting that the blend with PAH prevents an accurate measurement (see section 3.2.3).

5.4. *PAHs and IRS continuum*

The left panel of Figure 4.2 shows a detailed comparison MIR *Spitzer* spectrum and the model. The continuum and PAH features up to 13 μm are well fitted by the starburst model. At wavelengths longward of 13 μm, while the predicted continuum matches fairly well that observed, the predicted PAH features are in disagreement with those observed, both in central wavelength and strength. Only the 16.4 μm feature is reproduced.

We recall that our model for PAH emission is based on the Li & Draine (2001) model, which predicts PAH features at 3.3, 6.2, 7.7, 8.6, 11.3, 11.9, 12.7, 16.4, 18.3, 21.2, and 23.1 μm. The model of PAH features at $\lambda < 13$ μm was based on ISO data for the diffuse galactic medium. While the FWHM and the cross sections for the features at $\lambda > 13$ μm were taken from the theoretical study of 40 families of PAHs driven by Moutou et al. (1996), because of the lack of corresponding observational data.

More recently, ISO extended the observed wavelength range, and confirmed the feature at 16.4 μm, and also found new features at 14.2 and 17.4 μm, as well as a weak plateau between 15 and 20 μm (Moutou et al. 2000; Sturm et al. 2000; Van Kerckhoven et al. 2000). This plateau is attributed to a blend of many emission features provided by the interstellar PAH families present in the sources, and its variation can be accommodated by variations in the PAH populations (Peeters et al. 2004a). Lately, the higher sensibility of *Spitzer* confirmed the existence of PAH features at 14.2, 16.4 and 14.7 μm, and a new and prominent feature at 17.1 μm, among other weaker ones (e.g. Brandl et al. 2004; Smith et al. 2004; Werner et al. 2004). However, the lack of features at 18.3 μm, 21.2 μm, and 23.1 μm has been confirmed.

The disagreement between model and data was already noticed by Peeters et al. (2004b), Smith et al. (2004) and Dale et al. (2005) who, on the other hand, found very good agreement between the Li & Draine model and the data for $\lambda < 13$ μm. They attributed the disagreement at wavelengths longward of 13 μm to the large PAH sensitivity to their global molecular structure, since they involve the motion of the molecules as a whole, and therefore, they are very dependent on the exact PAH species in the emitting source.

Work is in progress to improve our PAHs emission model based on new *Spitzer* observations.

5.5. *Total aperture SED*

We have also compared our models with the total aperture SED of the galaxy. The total aperture SED includes the U, B, V, J, H, and K bands from GOLDMINE[8]; the LW2 (6.75 μm) and LW3 (15 μm) ISO bands from Boselli et al. (2003); the UV (2000Å) from Deharveng et al. (2002), all IRAS bands (with the exception of 25 μm), and the radio measurement described in section 4. These data are complemented by our IRAC flux measurements and GALEX data for the full aperture. The data are reported in table 6.

[8] Galaxy On Line Database Milano Network, http://goldmine.mib.infn.it

TABLE 6
Total aperture broad band fluxes of NGC 4435

λ (μm)	Band / Instrument	Flux (Jy)	Uncert. (mJy)	Ref.
0.2000	UV	3.4E-4	0.1	1
0.3601	U	0.0219	4.38	2
0.4399	B	0.0870	13.05	2
0.5500	V	0.166	24.9	2
1.25	J	0.61	122.0	2
1.65	H	0.70	105.0	2
2.17	K	0.53	106.0	2
3.6	IRAC	0.32	32.0	3
4.5	IRAC	0.18	18.0	3
5.8	IRAC	0.16	16.0	3
6.75	LW2	0.12	4.61	4
8.0	IRAC	0.16	16.0	3
12	IRAS	0.130	29.2	5
15	LW3	0.0765	8.73	4

References. — (1) Deharveng et al. 2002; (2) Goldmine; (3) this work; (4) Boselli et al. 2003; (5) NED.

Note. — Complementary IRAS and radio fluxes were already reported in Table 2.

The fit to the total aperture SED was done simply by changing the amount of the old stellar population and using the same starbust component that fits the central SED, as derived in the previous sections.

The resulting total mass of the old stellar population is $\mathrm{M}^{\mathrm{Tot}}_{\mathrm{old}} = 4.66 \times 10^{10}$ $M_{\odot}$. Moreover, the star forming component emits 8% of the total bolometric luminosity of the galaxy, while its stellar mass is only 0.3% of the total stellar mass of the galaxy. It is worth noting that the starburst in N4438 (the late type companion) accounted for a smaller fraction (about 0.1%) of its total stellar mass (Boselli et al. 2005).

The comparison between the observed full aperture SED and the model is shown in the Figure 6. The full aperture SED is well reproduced at all wavelengths. We stress that the old stellar component provides a significant contribution to GALEX, ISO LW2, LW3 and IRAS 12μm broad band fluxes.

5.6. *X-rays*

As a final step in the SED analysis we briefly consider the X-ray emission of NGC 4435, observed with *Chandra* by Machacek et al. (2004). The X-ray spectrum was fitted with a thermal component in the soft (0.3-2 keV) band attributed to hot gas, and a non-thermal component responsible for the 2-10 keV band emission. The hard component, with a luminosity of $L_{\mathrm{X}} = 3.9 \times 10^{32}$ W, is mostly concentrated within 3″ from the galaxy center. This emission was attributed to a possible low luminosity AGN (as suggested by Ho et al. 1997) plus recent star formation activity.

The observed hard X-ray luminosity of NGC 4435 is about five times larger than that expected from the

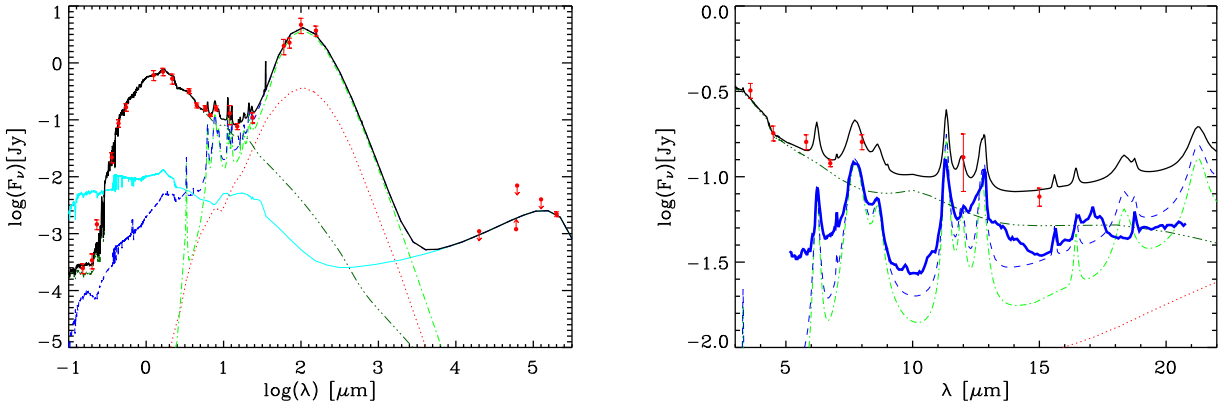

FIG. 6.— Comparison between the total aperture SED of NGC 4435 and the best fitting model. See Figure 4.2 for the description of different lines. *Left*: Comparison from 0.1μm to 100 MHz. *Right*: Comparison for the MIR wavelengths. The thickest solid line represents the IRS *Spitzer* spectrum.

FIR luminosity and the X-ray – FIR correlation found for starbursts galaxies (Ranalli et al. 2003). Moreover, adopting the calibration by Ranalli et al. (2003), the SFR implied by the observed hard X-ray luminosity turns out $\mathrm{SFR}_{\mathrm{X-ray}} = 0.78\ M_\odot\ \mathrm{yr}^{-1}$, one order of magnitude higher than the current SFR derived from the fit to the global SED.

Though this seems to support the AGN nature of the hard emission component we need to consider the peculiar star formation history of NGC 4435. In fact, due to the much higher SFR at the beginning of the burst, the average SFR is consistent with the X-Ray estimate. For this reason we expect a significant contribution to the X-Ray luminosity from intermediate mass stars accreting onto neutron stars and/or black holes, through Roche-lobe mass transfer. To check this possibility we have computed the X-ray emission expected from the star formation activity derived previously, with the synthesis model of Silva et al. (2003). The resulting value is consistent with the observed hard X-ray luminosity of NGC 4435. Moreover, we notice that the X-ray luminosity is much less dependent on the age of the stellar population (the turn-off mass of the stars) than the FIR luminosity. This implies that, in post starburst galaxies, the X-ray – FIR luminosity ratio tends to be larger than that of pure starbursts which are dominated by massive stars.

Another indication of the strength of the AGN comes from the comparison of the hard X-ray luminosity and Hα emission. Using the relation between L_{X}-$L_{\mathrm{H}\alpha}$, derived for AGN (Ho et al. 2001), the expected Hα luminosity would be $L_{\mathrm{H}\alpha}^{\mathrm{AGN}} \sim 6.6\times10^{31}$ W. This value is about 15% of the observed $L_{\mathrm{H}\alpha}$ corrected for extinction via the Balmer decrement. This contribution to the ionizing flux is higher than the limit derived from mid infrared nebular lines (Sect. 3.2.1). However it must be considered as a generous upper limit because on one hand all the X-ray luminosity has been attributed to the AGN and, on the other, it is known that the Balmer decrement provides only a lower limit to the attenuation (e.g. Panuzzo et al. 2003). In fact if we correct the observed $L_{\mathrm{H}\alpha}$ with the attenuation derived from our best fit model we obtain an upper limit to the AGN contribution ∼5%, consistent with what is found from the [Ne III]/[Ne II] ratio.

5.7. *NGC 4435 and the phenomenology of the galaxy-galaxy interaction*

NGC 4435 is interacting with NGC 4438; in particular, simulations by Vollmer et al. (2005) suggest that NGC 4435 passed through the disk of NGC 4438 about 100 Myr ago at a radial distance of 5-10 kpc. With such an impact parameter the interaction of the ISM of the two galaxies is unavoidable.

The age of the starburst t_{b} derived from our fit is larger than the (dynamically estimated) time since the ISM-ISM collision (around 100 Myr), but it is consistent with the epoch of the onset of interaction. This suggests that the star formation was triggered by the interaction (as often seen in galaxy-galaxy simulations, e.g. Barnes 2004) possibly producing a relevant activity also before the ISM-ISM collision. We cannot, however, draw strong conclusions on the relative importance of the tidal interaction and ISM-ISM collision, because it is difficult to derive the detailed shape of the star formation history during the burst.

Another phenomenon that may be triggered by galaxy-galaxy interaction is AGN activity (see e.g. Hopkins et al. 2006). However the various lines of evidence shown in this work indicate a lack of current AGN activity.

The age of the circumnuclear starburst is several times larger than the typical duration of the AGN phase and we cannot rule out the possibility that an AGN was once active in NGC 4435. However the surrounding gas is predominantly in a cold phase with only a fraction in a hot component ($\simeq 3\times10^7\ M_\odot$, Machacek et al. 2004), and it is supported by circular motion (Coccato et al. 2006), indicative of a relaxed ISM. We conclude that the feedback from the possible AGN was not strong enough to halt the star formation process which is now fading as a result of the gas consumption.

Alternatively, the AGN activity has not been triggered yet (and perhaps will not be triggered at all). Coccato et al. (2006) provide a 3σ upper mass limit of $7.5\times10^6\ M_\odot$ for the possible central SMBH, an order of magnitude lower than the value obtained from the M_{BH}-σ and M_{BH}-L_{bulge} relations. In this case NGC 4435 could be a prototype of the so called "laggard" SMBH which are believed to undergo slow gas fueling of the

galactic center and limited growth of the SMBH mass (Vittorini et al. 2005).

The above picture sketched for the evolution of NGC 4435 would suggest that the star formation activity could inhibit the AGN feeding both by consuming the gas and by SNe feedback. Both cases point towards a relatively low efficiency of the AGN feedback with respect to that of the SNe in intermediate/small mass galaxies like NGC 4435 (see e.g. Granato et al. 2004).

6. CONCLUSIONS

We have performed a thorough spectrophotometric study of the early-type galaxy NGC 4435 using new *Spitzer* IRS spectra combined with IRAC and MIPS archival data and existing broad band measurements from X-ray to radio wavelengths.

The IRS spectrum is dominated by PAH features, nebular emission lines and molecular hydrogen rotational lines that originate in the circumnuclear disk that characterizes this galaxy.

The PAH features in the spectrum are very similar to those observed in other star forming galaxies. In particular, we report the detection of the PAH feature observed at 17.1 μm (Smith et al. 2004) which, due to the lower contamination by the H_2 S(1) rotational line, we show is actually a blend of two distinct components.

The panchromatic SED of the central $5''$ region was analysed with the spectrophotometric code GRASIL.

This SED is well reproduced from the UV to radio by a model of a fading starburst superimposed on a simple stellar population of 8 Gyr and solar metallicity.

The analysis of MIR nebular lines, combined with that of the SED, allow a *direct* estimate of the gas metallicity, which also results as solar.

Though a low level nuclear activity has been suspected in NGC 4435 from optical (Ho et al. 1997, 2002) and X-ray (Machacek et al. 2004) observations, we collect the following evidence for the lack of AGN excitation:

(i) we have not detected high excitation nebular emission lines in the MIR spectrum

(ii) the [Ne III]15.5/[Ne II]12.8 ratio constrains the contribution of a possible AGN to the ionizing flux to be less than 2%.

(iii) the upper limit on the temperature derived from H_2 S(1) and S(2) rotational lines is lower than expected for AGN excitation.

(iv) the X-ray emission is within the range expected from X-ray binaries from the starburst

The age of the starburst, 186 ± 37 Myr, corresponds to the epoch of the last encounter with NGC 4438 derived from dynamical simulations, suggesting that this interaction has triggered the observed star formation event (Combes et al. 1988). However we cannot draw strong conclusions on the relative importance of the tidal interaction and ISM-ISM collision, because of the difficulty in deriving the detailed shape of the star formation history during the burst.

The combination of *Spitzer* observations with the analysis of the complete SED allows an accurate determination of the mass and epoch of the rejuvenation episode. The mass of the starburst ($\sim 1.40 \times 10^8\ M_\odot$) corresponds to about 1.4% of the stellar mass sampled by the central 5 arcsec aperture. The young component makes the optical spectrum of NGC 4435 closely similar to a typical interacting early-type galaxy with inverted Ca II[H+K] lines (Longhetti et al. 1999; Sarzi et al. 2005) that will later turn into a typical *cluster* E+A galaxy. This study supports the notion that early-type galaxies with relatively strong hydrogen absorption features are due to recent small rejuvenation episodes, rather than being the result of delayed galaxy formation (Bressan et al. 1996).

Finally the total SED of NGC 4435 is fitted by simply adding to the starburst a larger fraction of the old stellar population. The starburst provides only 0.3% of the total stellar mass of the galaxy but 8% of the bolometric luminosity.

We are deeply indebted to A. Boselli and L. Cortese for having provided us Galex UV data points. We thank E. Corsini and L. Coccato for useful discussions and for the WFPC2 image of NGC 4435. We thank the anonymous referee for corrections and helpful comments. We thank L. Paoletti, A. Petrella and D. Selvestrel for their work on the Galsynth interface. A. B., G. L. G. and L. S. thank INAOE for warm hospitality. O. V. acknowledges the support of the PICS MEXIQUE 2174 and the Mexican CONACYT projects 36547 E and 39714 F. This work is based on observations made with the *Spitzer* Space Telescope, which is operated by the JPL, Caltech under a contract with NASA.

REFERENCES

Barnes, J. E. 2004, MNRAS, 350, 798
Becker, R. H., White, R. L., & Edwards, A. L. 1991, ApJS, 75, 1
Boselli, A., Sauvage, M., Lequeux, J., Donati, A., & Gavazzi, G. 2003, A&A, 406, 867
Boselli, A., et al. 2005, ApJ, 623, L13
Bower, R. G., Lucey, J. R., & Ellis, R. S. 1992, MNRAS, 254, 589
Brandl, B. R., et al. 2004, ApJS, 154, 188
Bressan, A., Chiosi, C., & Tantalo, R. 1996, A&A, 311, 425
Bressan, A., Granato, G. L., & Silva, L. 1998, A&A, 332, 135
Bressan, A., Aussel, H., Granato, G. L., Rodighiero, G., Panuzzo, P., & Silva, L. 2001, ApSSS, 277, 251
Bressan, A., Silva, L., & Granato, G. L. 2002, A&A, 392, 377
Bressan, A., Panuzzo, P., Buson, L., Clemens, M., Granato, G. L., Rampazzo, R., Silva, L., Valdes, J. R., Vega, O., & Danese L. 2006, ApJ, 639, L55
Burton, M. G., Hollenbach, D. J., & Tielens, A. G. G. 1992, ApJ, 399, 563
Capetti, A., & Balmaverde, B. 2005, A&A, 440, 73
Cardelli, J. A., Clayton, G. C., & Mathis, J. S. 1989, ApJ, 345, 245
Coccato, L., Sarzi, M., Pizzella, A., Corsini, E. M., Dalla Bontá, E., & Bertola F. 2006, MNRAS, 366, 1050
Combes, F., Dupraz, C., Casoli, F., & Pagani, L. 1988, A&A, 203, 9
Dale, D. A., et al. 2005, ApJ, 633, 857
Domingue, D.L., Sulentic, J.W., Xu, C., Mazzarella, J., Gao, Y., & Rampazzo R. 2003, AJ, 125, 555
Dressel, L. L., & Condon, J. J. 1978, ApJS, 36, 53
Elson, R. A. W., Fall, S. M., & Freeman, K. C. 1987, ApJ, 323, 54
Engelbracht, C. W., et al. 2006, ApJL, in press (astro-ph/0603551)
Ferland, G. J., Korista, K. T., Verner, D. A., Ferguson, J. W., Kingdon, J. B., & Verner, E. M. 1998, PASP, 110, 761
Förster Schreiber, N. M., Roussel, H., Sauvage, M., & Charmandaris, V. 2004, A&A, 419, 501
Genzel, R., et al., 1998, ApJ, 498, 579
Granato, G. L., Lacey, C. G., Silva, L., Bressan, A., Baugh, C. M., Cole, S., & Frenk, C. S. 2000, ApJ, 542, 710
Granato, G. L., De Zotti, G., Silva, L., Bressan, A., & Danese, L. 2004, ApJ, 600, 580

Ho, L. C., Filippenko, A. V., & Sargent, W. L. 1995, ApJS, 98, 477
Ho, L. C., Filippenko, A. V., & Sargent, W. L. 1997, ApJS, 112, 315
Ho, L. C., et al. 2001, ApJ, 549, L51
Ho, L. C., Sarzi, M., Rix, H.-W., Shields, J. C., Rudnick, G., Filippenko, A. V., & Barth, A. J. 2002, PASP, 114, 137
Hony, S., Van Kerckhoven, C., Peeters, E., Tielens, A. G. G. M., Hudgins, D. M., & Allamandola, L. J. 2001, A&A, 370, 1030
Hopkins, P. F., Hernquist, L., Cox, T. J., Di Matteo, T., Robertson, B., & Springel, V. 2006, ApJS, 163, 1
Kelson, D. D., et al. 2000, ApJ 529, 768
Kenney, J. D. P., Rubin, V. C., Planesas, P., & Young, J. S. 1995, ApJ, 438, 135
Kennicutt, R. C. Jr. 1998, ARA&A, 36, 189
Kennicutt, R. C. Jr., et al. 2003, PASP, 115, 928
Kewley, L. J., Dopita, M. A., Sutherland, R. S., Heisler, C. A., & Trevena, J. 2001, ApJ, 556, 121
Kroupa, P. 1998, in ASP Conf. Ser. 134, Brown Dwarfs and Extrasolar Planets, ed. R. Rebolo, E. L. Martin & M. R. Zapatero Osorio (San Francisco: ASP), 483
Li, A., & Draine, B. T. 2001, ApJ, 554, 778
Longhetti, M., Bressan, A., Chiosi, C., & Rampazzo, R. 1999, A&A, 345, 419
Lutz, D., Kunze, D., Spoon, H. W. W., & Thornley, M. D. 1998, A&A, 333, 75
Machacek, M. E., Jones, C., & Forman, W. R. 2004, ApJ, 610, 183
Moutou, C., Leger, A., & D'Hendecourt, L. 1996, A&A, 310, 297
Moutou, C., Verstraete, L., Léger, A., Sellgren, K., & Schmidt, W. 2000, A&A, 354, 17
Nagar, N. M., Falcke, H., Wilson, A. S., & Ho, L. C. 2000, ApJ, 542, 186
Panuzzo, P., Bressan, A., Granato, G. L., Silva, L., & Danese, L. 2003, 409, 99
Panuzzo, P., Silva, L., Granato, G. L., Bressan, A., & Vega, O. 2005, in AIP Conf. Proc. 761, The Spectral Energy Distributions of Gas-Rich Galaxies: Confronting Models with Data, ed. Popescu C. C. & Tuffs R. J., 187
Panuzzo P., Granato, G. L., Buat, V, Inoue, A. K., Silva, L., Iglesias-Páramo, J., & Bressan, A. 2006, MNRAS, submitted
Parmar, P. S., Lacy, J. H., & Achtermann, J. M. 1991, ApJ, 372, 25
Peeters, E., Mattioda, A. L., Hudgins, D. M., & Allamandola, L. J. 2004a, ApJ, 617, L65
Peeters, E., Spoon, H. W. W., & Tielens, A. G. G. M. 2004b, ApJ, 613, 986
Ranalli, P., Comastri, A., & Setti, G. 2003, A&A, 399, 39
Rigopoulou, D., Kunze, D., Lutz, D., Genzel, R., & Moorwood, A. F. M. 2002 A&A, 389, 374
Robin, A. C., Reylé, C., Derrière, S., & Picaud, S. 2003, A&A, 409, 523
Roussel, H., Sauvage, M., Vigroux, L., & Bosma, A. 2001, A&A, 372, 427
Salpeter, E. E. 1955, ApJ, 121, 161
Sandage, A., & Tamman, G. A. 1981, Revised Shapley-Ames Catalog of Bright Galaxies (Carnegie Inst. of Washington)
Sarzi, M., Rix, H. W., Shields, J. C., Ho, L. C., Barth, A. J., Rudnick, G., Filippenko, A. V., & Sargent, W. L. W. 2005, ApJ, 628, 169
Silva, L., Granato, G. L., Bressan, A., & Danese, L. 1998, ApJ, 509, 103
Silva, L. 1999, PhD Thesis, SISSA, Trieste, Italy
Silva, L., Granato, G. L., Bressan, A., & Panuzzo, P. 2003, RevMexAA Conf. Ser., 17, 93
Smith, J. D. T., et al. 2004, ApJS, 154, 199
Sturm, E., Lutz, D., Tran, D., Feuchtgruber, H., Genzel, R., Kunze, D., Moorwood, A. F. M., & Thornley, M. D. 2000, A&A, 358, 481
Van Kerckhoven, C., et al. 2000, A&A, 357, 1013
Vega, O., Silva, L., Panuzzo, P., Bressan, A., Granato, G. L., & Chavez, M. 2005, MNRAS, 364, 1286
Verma, A., Lutz, D., Sturm, E., Sternberg, A., Genzel, R., & Vacca, W. 2003, A&A, 403, 829
Veilleux, S., & Osterbrock, D. E. 1987, ApJS, 63, 295
Vittorini, V., Shankar, F., & Cavaliere, A. 2005, MNRAS, 363, 1376
Vollmer, B., Braine, J., Combes, F., & Sofue, Y. 2005, A&A, 441, 473
Werner, M. W., Uchida, K. I., Sellgren, K., Marengo, M., Gordon, K. D., Morris, P. W., Houck, J. R., & Stansberry, J. A. 2004, ApJS, 154, 309
Wrobel, J. M., & Heenschen, D. S. 1991, AJ, 101, 148
Witt, A. N., & Gordon, K. D. 2000, ApJ, 528, 799